Quantified Pore-Scale Nanoparticle Transport in Porous Media and the Implications for Colloid Filtration Theory

Quantified pore-scale nanoparticle transport in porous media and the implications for colloid filtration theory

Ian L. Molnar[1], Paula Sanematsu[2], Jason I. Gerhard[1], Clinton S. Willson[3] and Denis M. O'Carroll[1,4*]

[1]Department of Civil and Environmental Engineering, The University of Western Ontario, London, ON, Canada N6A 5B9

[2]Craft and Hawkins Department of Petroleum Engineering, Louisiana State University, Baton Rouge, LA 70803

[3]Department of Civil and Environmental Engineering, Louisiana State University, Baton Rouge, LA 70803

[4]School of Civil and Environmental Engineering, Connected Water Initiative, University of New South Wales, Manly Vale, NSW, 2093, Australia

[*]Corresponding author.

Denis M. O'Carroll: Tel +61 2 8071 9800

e-mail: docarroll@eng.uwo.ca

Abstract

This study evaluates the pore-scale distribution of silver nanoparticles during transport through a sandy porous medium via quantitative Synchrotron X-ray Computed MicroTomography (qSXCMT). The associated distribution of nanoparticle flow velocities and mass flow rates were obtained by coupling these images with Computational Fluid Dynamic (CFD) simulations. This allowed, for the first time, the comparison of nanoparticle mass flow with that assumed by the standard Colloid Filtration Theory (CFT) modelling approach. It was found that (i) 25% of the pore space was further from the grain than assumed by the CFT model; (ii) Average pore velocity agreed well between results of the coupled qSXCMT/CFD approach and the CFT model within the model fluid envelope, however, the former were 2 times larger

than the latter in the centers of the larger pores and individual velocities were upwards of 20 times those in the CFT model at identical distances from grain surfaces

; and (iii) Approximately 30% of all nanoparticle mass and 38% of all nanoparticle mass flow occurred further away from the grain surface than expected by the CFT model. This work suggests that a significantly lower fraction of nanoparticles will contact a grain surface by diffusion than expected by CFT models, likely contributing to inadequate CFT model nanoparticle transport predictions.

Introduction

Predicting the transport of Engineered Nanoparticles (ENPs) through the subsurface is an important and unresolved topic. ENPs are widely used in both industrial processes and consumer products[1]; their prevalence suggests the likelihood of their presence in the subsurface and, if mobile, may pose risks to municipal drinking water supplies or surface water bodies. Engineered nanoparticles, such as nano-Zero-Valent-Iron (nZVI), are also being purposely injected into the subsurface at contaminated industrial sites to degrade contaminants [2]. As a result, accurately predicting the transport of ENPs through soil is valuable for both groundwater source zone protection and designing efficient site-remediation schemes.

However, current modelling approaches cannot adequately simulate nanoparticle transport through soil[3]. The classic approach to continuum-scale modelling of nanoparticle transport employs the Advection-Dispersion Equation (ADE) with a first-order kinetic retention coefficient (k_{att})[4] , which predicts a symmetric breakthrough concentration curve and a log-linear concentration profile of retained nanoparticles[4]. However, nanoparticle transport experiments generally exhibit non-symmetrical breakthrough curves with extended tailing behavior[5, 6, 7, 8, 9, 10]

and retention profiles that are either hyperexponential [5, 6, 11, 12, 13, 14, 15, 16, 17, 18, 19] or non-monotonic [11, 12, 13, 14, 16, 17, 19, 20, 21, 22, 23]. The fundamental mechanisms driving these anomalous nanoparticle transport behaviours have not yet been definitively identified as there is a poor understanding of the pore-scale distribution and behavior of nanoparticles during transport in real porous media [4]. This lack of pore-scale knowledge hinders the development of models that can accurately describe, and predict, nanoparticle transport through soil.

The most common mechanistic model to predict k_{att}, Colloid Filtration Theory (CFT), has been employed for a wide range of nanoparticles and environmental conditions[15, 24, 25, 26, 27, 28, 29, 30, 31, 32, 33, 34, 35]. CFT's mechanistic model employs a force/torque balance to calculate colloid trajectories and attachment in the presence of a collector (or assemblage of collectors) to determine the fraction of approaching colloids which contacts the collector surface: the 'contact efficiency', η. The specific forces and torques, and boundary conditions, employed by each CFT model is discussed in detail elsewhere [4]. The CFT-predicted η is then upscaled into the continuum-scale k_{att} by applying a colloid mass balance over a continuum control volume filled with identical collectors.

There are a number of different CFT mechanistic models that employ different force/torque balances, environmental conditions and model geometries [36, 37, 38, 39, 40, 41]. A key consideration is the Derjaguin-Landau-Verwey-Overbeek (DLVO) condition: favorable DLVO conditions refer to scenarios with no repulsive energy barrier preventing attachment of the colloid onto the grain. Under favorable DLVO conditions, CFT mechanistic models generally well describe micron-sized colloid retention[4], but over-predict nanoparticle retention [8, 38]. It should be noted that this over-prediction is different from the phenomenon of CFT models predicting η values greater than 1 at very low fluid velocities, which a number of recent studies

have attempted to address [38, 42, 43]. The over-prediction of nanoparticle attachment discussed in this study is an over-prediction relative to experimental observations which appears even in the CFT models and correlation equations that have been specifically modified to prevent η values greater than 1[38]. For unfavorable DLVO conditions, CFT models are unable to predict experimental retention rates for micron or nano-sized particles[44] due to the presence of a repulsive DLVO energy barrier which prevents direct attachment of the colloid onto the collector surface. The most common approach to adapting CFT for use in unfavorable conditions is to fit k_{att} to experimental results via an additional parameter: α, 'attachment efficiency'. The α parameter acts as a multiplier for η (which was derived assuming favorable conditions) to describe the fraction of nanoparticles contacting a collector surface that remain attached to the surface in unfavorable conditions. This modified 'αη' parameter is adjusted until the model result matches up with the experimental observations. However, by employing α as a multiplier for η, studies that attempt to predict α or examine the influence of parameters on α are limited by the implicit assumption that CFT is able to accurately predict η.

It has been hypothesized that CFT's over-prediction of η relative to experimental observations for nanoparticles is due, in part, to the mechanistic models' assumptions about pore and grain geometry[8, 45, 46]. The typically assumed geometry is a perfectly spherical collector (i.e., grain) surrounded by a shell of fluid – termed the Happel Sphere-In-Cell (HSIC) [37, 38, 40, 47, 48]. Recently, Molnar et al. [49] developed a quantitative-Synchrotron X-ray Computed MicroTomography technique (qSXCMT) to determine the pore-scale concentration distribution of nanoparticles in soil columns during transport experiments. The qSXCMT method was then used by Molnar et al. [8] to illustrate how CFT's over-prediction of η for nanoparticles could be linked to regions of relatively low fluid velocity near grain-grain contacts, a feature not

94 accounted for within the HSIC geometry. The study also linked these low velocity regions to the
95 extended tailing behavior often observed in nanoparticle experiments [8].

96 However, other simplifying assumptions within the HSIC geometry may be further
97 preventing CFT models from accurately predicting nanoparticle transport. For one, it assumes
98 the average flow field through a realistic porous medium can be approximated by the analytical
99 solution of creeping flow through the Happel fluid envelope. As well, it approximates the pore-
100 space as a narrow shell of fluid through which all nanoparticles flow. A number of studies have
101 indicated that realistic flow fields may not be consistent with CFT[8, 50, 51, 52]. However, these pore-
102 scale assumptions, fundamental to the HSIC geometry and thus CFT predictions, have never had
103 their validity tested for actual nanoparticle transport through real porous media.

104 In this study, qSXCMT and Computational Fluid Dynamics (CFD) are employed to
105 determine, for the first time, the averaged distribution of nanoparticle mass *flux* (mass flow per
106 unit area, italicized to avoid confusion with mass flow) and flow rates within a soil's pore spaces.
107 qSXCMT was coupled with CFD to characterize the averaged pore-scale nanoparticle
108 distribution and flow field during a nanoparticle column transport experiment. A silver
109 nanoparticle solution was injected into a column packed with uniform quartz sand under
110 unfavorable DLVO conditions and was imaged via qSXCMT at regular intervals during
111 nanoparticle injection and elution. First, this study computationally characterized the distribution
112 of pore space within the soil and examined how well experimentally determined, bulk-measured
113 lab properties (i.e., soil sieve analysis) described the imaged pore and grain geometry. Then, the
114 distribution of fluid velocity through the soil was estimated via CFD simulations and compared
115 to analytical solutions for creeping flow in the HSIC geometry. Next, the distribution of
116 nanoparticle mass within the pore space was determined by qSXCMT and coupled with the

CFD-simulated velocity distribution to estimate silver nanoparticle mass *flux* and mass flow rate distributions. The findings provide some of the first experimental insights into how pore-scale nanoparticle behaviour impacts continuum-scale transport as well as yielding significant insight into why predicting nanoparticle transport remains a challenge for CFT.

Materials and Methods

A silver nanoparticle (nAg) transport experiment was undertaken at the GeoSoilEnviro Center of Advanced Radiation Sources (GSECARS) 13-BM-D beamline at the Advanced Photon Source, Argonnne National Lab. The experimental method is described in detail in Molnar et al. [8]; a summary of the relevant details are provided here. Note that the nAg transport experiment and corresponding SXCMT datasets examined here were also used in Molnar et al. [8], there described as the 'Uniform Quartz' dataset. The analysis presented here is entirely new; this paper does not re-use or re-present any results from the Molnar et al. [8] study.

Materials

Silver nanoparticles were synthesized by reducing silver nitrate (0.1N, Alfa Aesar) with sodium borohydride (Granulated, 97+%, Alfa Aesar) and electrosterically stabilized with a 1% solution of carboxymethylcellulose 90k (CMC90k). The synthesis procedure is discussed in detail elsewhere [8, 49]. CMC90k is a polymer that is typically employed to stabilize bi-metallic particles (i.e. nZVI) for site remediation due to its superior stabilization[2, 53, 54]. Previous studies have employed CMC90k as an nAg stabilizer and discuss its nAg-stabilization properties in greater detail [8, 49]. It has been shown that CMC90k does not compete with nAg for deposition

sites and does not alter nAg deposition rates onto the quartz surface [8]. The synthesis procedure occurred at the GSECARS wet lab the day before the allotted synchrotron beam time. The synthesized silver nanoparticles were analyzed via Dynamic Light Scattering and were found to have an average hydrodynamic diameter (d_{50}) of 29.8 nm and a zeta potential of -27.97 mV. The viscosity of the final CMC90k stabilized solution was 14 cP. An additional solution of silver nanoparticles was synthesized using an identical method for the purpose of TEM imaging. Approximately 24 hours elapsed between the second solution synthesis and creating the TEM grids to be consistent with the time between initial synthesis and qSXCMT imaging. The resulting TEM image is presented in Molnar et al [8]. A size analysis of the particles within the TEM image was conducted using ImageJ which identified 85 nanoparticles with an average diameter of 13.8 nm (maximum: 61.9 nm, minimum: 1.6 nm) and a standard deviation of 12.3 nm.

The porous medium employed for the transport experiment was a quartz sand (Unimin Accusand) that had been cleaned by rinsing with Nitric Acid (Environmental grade, Alfa Aesar) followed by rinsing with deionized water and left to dry overnight. The sand was sieved to achieve a specific grain size distribution (420 – 600 μm) and was then wet-packed into a small aluminum column (ID: 5.6 mm, length: 5 cm). Rigorous packing procedures (which included stirring, vibrating and tamping) were undertaken to ensure that the column was uniformly packed throughout and to avoid edge effects throughout the column. The solution used for wet packing contained no nanoparticles but was controlled to the same viscosity (i.e. 1% CMC90k solution at 14 cP) and ionic strength (120 mM, achieved with Sodium Nitrate) as the nAg solution. The porosity of the column (33%) was determined by measuring the specific gravity of the sand (2.65 g/cm^3) and weighing the amount of sand packed into the column.

161 Standard DLVO theory was used to estimate the DLVO energy profile for the uniform
162 quartz sand and is described in detail in Molnar et al.[8]. Briefly, the zeta potential for the quartz
163 sand was taken from literature values to be -55 mV[12] as it was found to have little impact on the
164 DLVO profile. The calculated DLVO profile, presented in Molnar et al [8], indicated that the
165 quartz sand was unfavorable to silver nanoparticle attachment in the experimental conditions and
166 contained a small repulsive energy barrier with a magnitude of 8.5 kT.

167 Silver nanoparticle transport experiment

168 The packed column was loaded into the imaging hutch and a pre-injection image was
169 collected. Following pre-injection imaging, the silver nanoparticle solution was injected with a
170 syringe pump at 0.11 mL/min. The flow direction was upwards through the column. A total of 3
171 pore volumes (PV's) of nAg solution was injected into the column and qSXCMT imaging
172 occurred at 0.25, 0.5, 0.75, 1 and 2 PV's of injection. The column was imaged at its midpoint,
173 2.55 cm above the base of the porous medium. The length of column section imaged (referred to
174 as the 'SXCMT imaging window') was 0.51 cm and extended from 2.55 cm to 3.06 cm above
175 the base of the column. The concentration of silver nanoparticles in the injection solution was
176 measured at the beginning and end of the nAg injection period via acid-digestion and ICP-OES
177 analysis. The average silver nanoparticle concentration being injected into the column was
178 determined to be 2.48 g/L (+/- 0.06 g/L).

179 After injecting 3 PV's of the nAg solution, the input was switched to a 1% CMC90k
180 solution with no silver nanoparticles – controlled to the same pH and ionic strength as the wet
181 packing and nAg solutions – to flush the nanoparticles out of the column. The column was
182 imaged after 1 and 2 PV's of elution and elution continued for an additional 5 PV's (7 PV's of

183 elution total) with no additional qSXCMT imaging. During injection and elution, samples were
184 collected from the column's effluent and analyzed for total silver concentration via ICP-OES
185 and, following the experiment the sand was acid-digested to test for retained nanoparticle
186 concentration. The results from the effluent sampling and acid-digestion are presented elsewhere
187 [8].

188 It should be noted that the results of this study are presented in terms of SXCMT pore
189 volumes (SXCMT-PV's) injected, not total column pore volumes. An SXCMT-PV is defined as
190 the pore space between the bottom of the column and the center of the imaging window
191 (approximately 0.22 mL) whereas a total column pore volume (PV's) refers to the pore volume
192 of the entire column (approximately 0.4 mL). Thus '1 SXCMT-PV's injected' refers to when the
193 advective front of the injected nAg solution reaches the center of the SXCMT imaging window.
194 qSXCMT imaging occurred at 0.4, 0.9, 1.3, 1.8, 3.6, 7.2 and 8.9 SXCMT-PV's corresponding to
195 0.25, 0.5, 0.75, 1, 2, 4 and 5 total column pore volumes. Incorporating these separate definitions
196 of pore volumes allows for a comparison of the relative position of the advective front of the
197 injected nAg solution to the SXCMT imaging window and the column's effluent.

198 ## SXCMT imaging, reconstruction and analysis

199 The specific imaging procedure required for qSXCMT imaging of silver nanoparticles in
200 a porous medium is discussed in detail elsewhere [8, 49]. Briefly, during qSXCMT imaging all flow
201 through the column was stopped, approximately 40 min/dataset; this stoppage time has no impact
202 on pore-scale nAg distribution[8].The column was then imaged four times in a single location to
203 collect four datasets of linear mass attenuation values at different x-ray energies above and below
204 the silver K-edge of 25.514 keV. The voxel resolution of the collected images was determined to

be 9.87 μm/voxel. Image reconstruction produced a 3-dimensional dataset of x-ray linear mass attenuation values averaged over a 9.87×9.87×9.87 μm^3 voxel.

Sub-volumes of 350×350×450 voxels were cropped from the reconstructed datasets at each time-step (40 minute imaging period) to remove edge effects and column material and underwent a segmentation into water and solid using an indicator kriging technique [55, 56]. Grain characteristics and pore-network structure within each segmented image were then extracted and characterized using the method of Thompson et al. [57, 58]. This method assigns a unique identifier to every pore and grain within the segmented sub-volumes as well as topological properties. The three-dimensional segmented sub-volume of the pre-injection dataset, as well as a two-dimensional slice of raw reconstructed gray values, are presented in Figure S1 (supplementary information) to illustrate the structure of the porous medium within the SXCMT imaging window. In addition, an algorithm was employed for each imaged time-step to measure the distance between each pore space voxel and the closest grain surface voxel (see supplementary information).

Quantifying silver nanoparticle concentrations within the SXCMT sub-volumes

The method of Molnar et al. [49] was employed to calculate the qSXCMT-determined silver nanoparticle concentration for each pore-space voxel in the cropped sub-volume for the above-mentioned time-steps. Briefly, for each time-step the below-edge dataset (25.414 keV) was subtracted from each of the 3 above-edge datasets (25.614, 25.714, 25.814 keV) to create 3 difference datasets. Then, using the solid/pore segmented datasets created earlier, a modified form of the Beer-Lambert law [49] was applied to every single pore-space voxel in all 3 difference datasets to create 3 unique ‘SXCMT-determined concentration’ datasets for silver nanoparticles.

The 3 datasets were averaged together to create 1 final SXCMT-determined nanoparticle concentration dataset for each imaged time-step. Each of the qSXCMT-determined datasets (corresponding to each imaged time-step) were calibrated using a previously created calibration procedure described in Molnar et al. [8]. This qSXCMT procedure does not accurately determine nanoparticle concentration on a voxel-by-voxel basis due to noise associated with qSXCMT imaging. However, averaging the approximately 16 million voxels with various techniques can accurately quantify average spatial and temporal changes in nanoparticle concentrations within the bulk pore space at a resolution similar to the imaged resolution (10.47 μm/voxel)[8, 49]. Moreover, this qSXCMT method is currently unable to accurately determine nanoparticle concentrations within 17.3 μm of the grain surface due to a 'shadow zone' effect caused by x-ray refraction at the grain/pore interface (this width is experiment specific and should not be taken as a general value) [49]. Thus, all pore-space voxels within the 'shadow zone' in each qSXCMT-determined concentration dataset are discarded during this quantification and calibration process.

Fluid Dynamics Modeling within the Image-derived Pore Space

Computational Fluid Dynamics (CFD) modeling was employed to simulate fluid flow in a uniform quartz SXCMT dataset (referred to hereafter as the 'image-derived pore space' to avoid confusion with the qSXCMT datasets, see Figure S1). A single dataset was employed for CFD modeling (0 PV, i.e. pre-injection) as it can be assumed that the flow field did not change throughout the injection or elution period because the extracted pore network statistics were similar for all datasets.

First, unstructured tetrahedral meshes were generated using an in-house code[59, 60]. In order to assess if the simulated fluid flow was sensitive to mesh resolution, meshes of increasing

resolution were generated for a smaller domain (150×150×350 voxels) until flow rate and velocity profiles converged (i.e., no longer changed). Then, a resolution within the converged range that was also computationally feasible for the large domain (350×350×450 voxels) was used for the final mesh.

CFD modeling was conducted using an in-house three-dimensional Finite Element Method (FEM) algorithm [60, 61] which solves the Stokes equation on the unstructured mesh. Constant traction (normal component) boundary conditions (BCs) were applied at the inlet and outlet (top and bottom). From the constant traction, the corresponding pressures and pressure gradient were calculated. On the other four faces of the domain as well as on the solid-void surfaces inside the porous medium, no-slip BCs were imposed (roughness was not accounted in the model as the resolution of the SXCMT images cannot capture such features). More details on the implementation of FEM and its BCs can be found in [59, 60]. The FEM simulation reproduced the experimental conditions by matching all relevant experimental properties (e.g., viscosity) and by adjusting the inlet and outlet pressure BCs until the average velocity matched the average experimental pore water velocity of the column experiment.

In addition to flow rate and velocity profile convergence, confidence in the simulated flow field was developed by calculating soil permeability using Darcy's law. The simulated permeability (1.3×10^{-6} cm^2) is consistent with those experimentally determined for similarly sized sands (e.g., 6.4×10^{-7} cm^2 [62]). However, it is important to note that this only ensures that the average simulated flow properties are approximately consistent with the average experimental flow. This was deemed sufficient as this study focuses on average behavior and does not compare concentrations and simulated flow on a voxel-by-voxel basis.

It should be noted that no particle transport modeling was conducted. All estimates of nanoparticle flux and flow in this paper are the result of combining the CFD modeled flow field with the experimentally derived qSXCMT datasets of nanoparticle distribution.

Fluid Dynamics within the HSIC Geometry

An analytical solution was employed to solve for the fluid flow through the HSIC geometry. The flow regime through this geometry is assumed to be creeping flow and is described via the continuity and Stokes flow equations. The solution to the velocity vectors in the HSIC geometry are not explicitly published in any of the mechanistic model papers [37, 38, 40, 48, 63]. However, the general stream function and HSIC-specific coefficients published in Elimelech [63] can be used to solve for fluid velocities in the HSIC geometry.

Results

The results are divided into three sections. The first compares the HSIC geometry to the pore and grain network extracted from the image-derived pore space. The second compares the analytical solutions of fluid flow through the HSIC geometry to the CFD-simulated flow field in the image-derived pore space. The third examines the distributions of nAg mass, mass *flux* and mass flow in the SXCMT datasets. Throughout, the discussion considers whether the HSIC geometry is appropriate for approximating nanoparticle transport through a realistic porous medium.

HSIC vs. SXCMT pore and grain geometry

The computationally-determined porosity of the image-derived pore space (29%) is lower than the experimentally-determined packed column porosity (33%), however the values are similar enough that the computationally-determined SXCMT pore and grain statistics can be taken as approximately equivalent to the experimental column's pore and grain network. The computational grain and pore network statistics were compiled by examining 329 uniquely identified grains, 2,139 pore bodies and 26,362 pore throats (the narrow region connecting two pore bodies). The total number of grains and pores within the dataset is significantly larger (619 grains and 3,802 pores), however the extra grains and pores were excluded from the analysis as they intersected the dataset edges. The aspect ratio of each grain was determined computationally from the image-derived pore space by measuring the average ratio between the length of each grain's longest axis to its shortest. The average grain aspect ratio was 1.64 suggesting that the grains within the dataset were non-spherical which is qualitatively consistent with the images of the SCXMT dataset in Figure S1 and with previously published literature [64] of typical sandy media. The average pore inscribed radius is 59.4 μm and the average throat inscribed radius is 39.9 μm.

As mentioned, employing a CFT-HSIC mechanistic model (or η-correlation equation) to describe nanoparticle transport assumes that all fluid flow occurs within the envelope surrounding a spherical collector (illustrated in Figure S2 in the supplementary information). The width of this fluid envelope (r, Figure S2) is defined so that the porosity of the HSIC geometry (the volume ratio of fluid envelope volume/spherical collector volume) is equivalent to the macroscopic porosity of the porous medium and is calculated from eq. 1:

$$r = a_s(1-n)^{-1/3} - a_s \qquad \text{Eq. 1}$$

where a_s is the radius of the spherical collector and n is the porosity. This definition of the fluid envelope, along with eq. 1, is used throughout the CFT literature [37, 38, 40, 48, 63] as it is a relatively simple method for accounting for porosity as well as the influence of neighbouring collectors on the fluid velocity. Sieve analysis of the uniform quartz sand mixture determined the average radius of the sand (a_s = 255 μm). Thus the HSIC geometry, applied to this experiment via eq. 1, approximates all the pore space as being within a 36 μm-thick fluid envelop around the grain.

The HSIC envelope width (36 μm) is, in fact, more similar to the average pore throat radius (39.9 μm) than the average pore body radius (59.4 μm). This suggests that a majority of the uniquely identified pore bodies have some pore fluid volume that is at least 23 μm further away from a grain surface than considered by HSIC. The difference between average pore body width and HSIC fluid envelope width is illustrated by Figure 1.

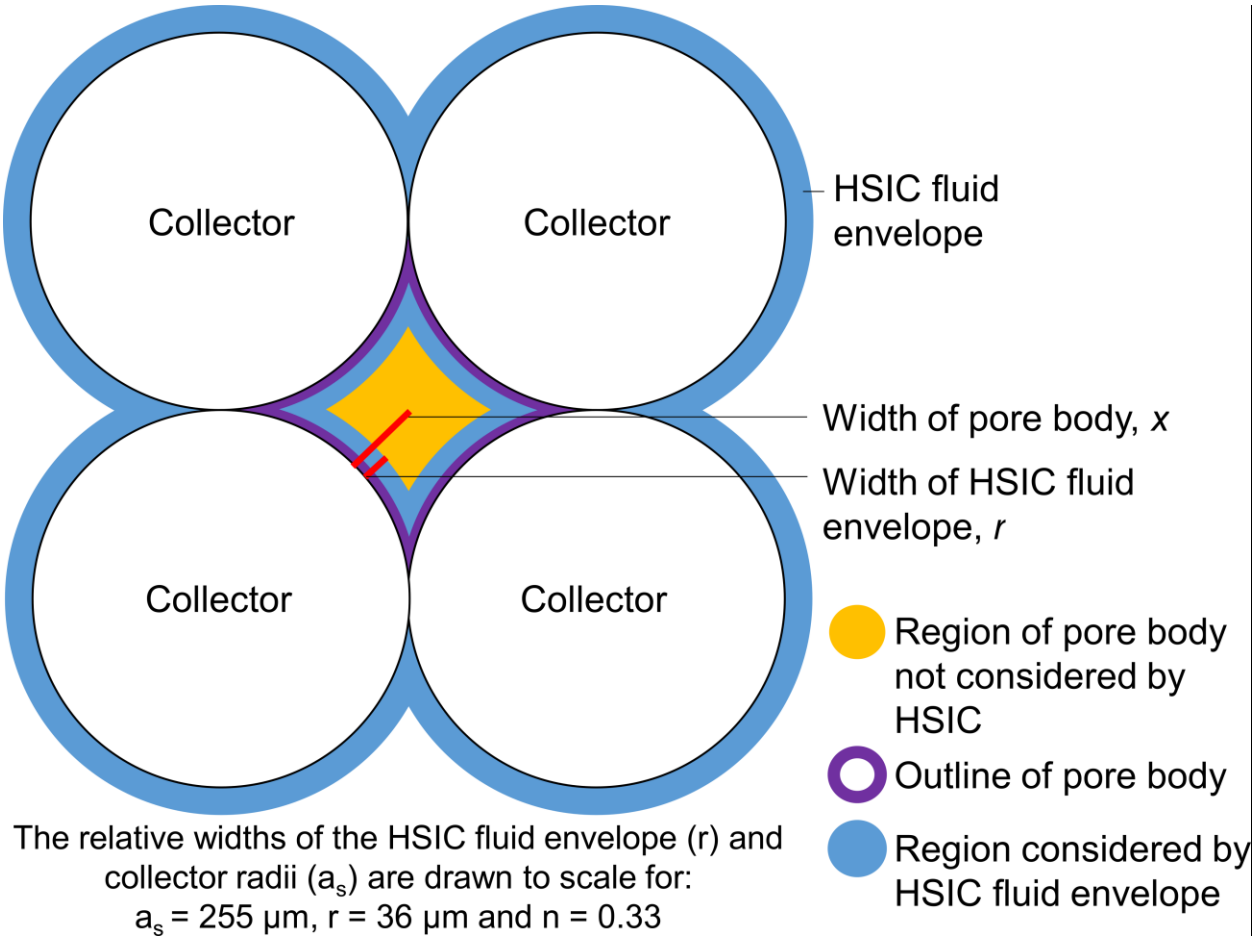

Figure 1: A depiction of how a pore body surrounded by a four circular collectors has a portion of pore space that is within the region considered by the HSIC's fluid envelope and a portion of pore space that is outside of the region considered by the HSIC fluid envelope.

The difference between the image-derived pore space's pore geometry and the HSIC is further highlighted by plotting the pore network and grain statistics as a cumulative percentage in Figure 2. The average Grain Effective Radius, 250 µm, was determined computationally from the image-derived pore space (defined as the average of the grain's short and long axis radii) and is consistent with the mean radius of sieved sand, 255 µm. It is also consistent, by extension, with the radius of the spherical collector in the HSIC geometry because the latter is set equal to the mean radius of sieved sand. The consistency between the HSIC collector radius and the average Grain Effective Radius suggests that (1) the image segmentation routine accurately

identified the boundary of the water/grain interface, and (2) the grains within the image-derived pore space are representative of the overall experimental column. In addition, the distribution of Grain Effective Radii within the image-derived pore space ranges from 200 – 300 μm (i.e., grain effective diameter = 400 – 600 μm) and is consistent with the sieved grain size distribution (420 – 600 μm). The Grain Effective Radius tailing towards 0 μm in Figure 2 is likely due to the fact that the cropping procedure for the network analysis could not remove all partial grains from the statistics analysis.

The distribution of pore bodies in Figure 2 suggests that of the identified 2,139 pores, approximately 80% have a radius equal to, or larger than, the width of the HSIC fluid envelope. Thus within 80% of pores, some fraction of nanoparticles will be further away from the grain surface than expected by CFT-HSIC models. The largest pore within the dataset has an inscribed radii of 160 μm, therefore nanoparticles can be upwards of 124μm further away from a grain surface than expected by CFT-HSIC. This trend is consistent with pore throats as well; of the 26,362 identified pore throats, approximately 50% are larger than the HSIC fluid envelope and can range up to 130 μm in radius.

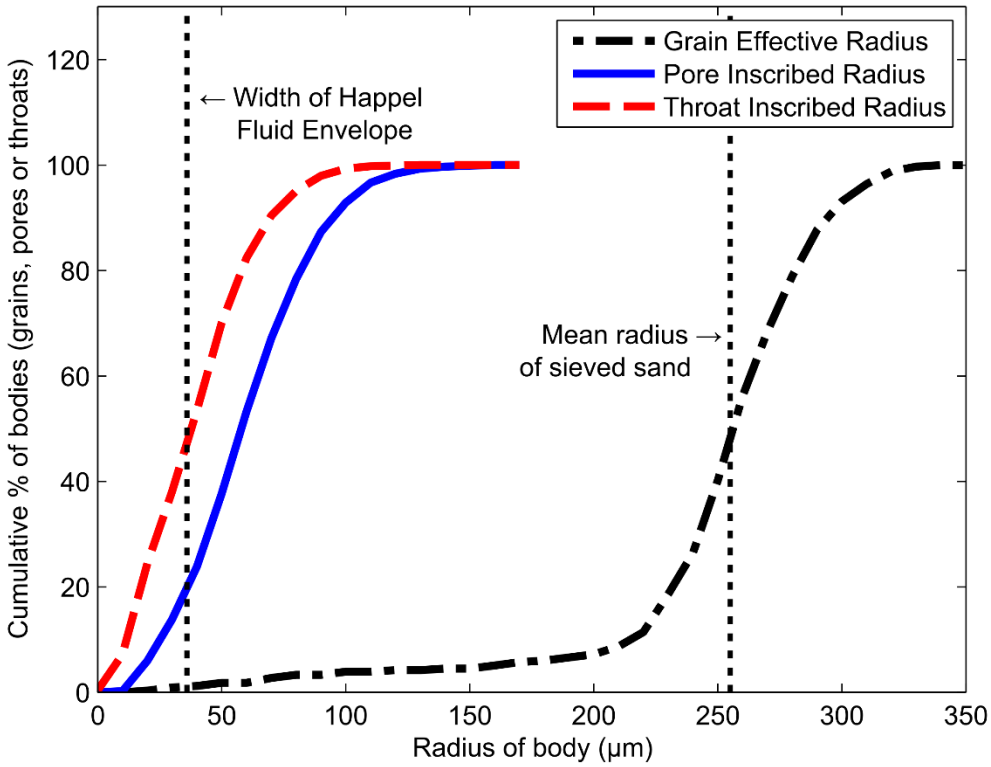

Figure 2: Cumulative size distributions of the grains (black), pores (blue) and pore throats (red) within the pore network of the image-derived pore space. Inscribed radius refers to the radius of the largest sphere that can be drawn entirely within the body. Effective radius is an average of the inscribed radius and the length of the grain's longest axis.

Figure 3 (top) illustrates how the volume of pore space in the image-derived pore space and HSIC geometry changes as a function of distance from the nearest grain surface. For the image-derived pore space, after determining the distance between each pore space voxel and the closest surface voxel, the distances were then sorted into bins representing 9.87 μm intervals from the grain surface (corresponding to the length of 1 voxel). The number of voxels in each bin was divided by the total number of pore space voxels to determine the percentage of pore space within each bin. To determine the distribution of pore space in the HSIC geometry, the volume of thin fluid shells were calculated in 9 μm intervals using the geometric equation for volume of a sphere (9 μm intervals were used instead of 9.87 so that 4 data points would not over-estimate the volume of HSIC pore space).

366 Figure 3 reveals that the volume of pore space in the image-derived pore space decreases
367 with distance from a grain surface, indicating that there is more pore space near the grain surface
368 than at the centers of the pores (qualitatively illustrated in Figure 1). This decreasing trend in the
369 real porous media is the opposite of what is encountered within the HSIC geometry. The trend
370 of increasing pore space volume with distance arises from the HSIC conceptual model; since the
371 volume of a sphere is a cubed function of its radius, the pore space volume in the HSIC geometry
372 is greatest at the outer edge of the fluid envelope. In Figure 3 (bottom), these trends are plotted
373 as a cumulative percentage of total pore space (total percentage of pore space closer to the grain
374 surface than a certain distance). It demonstrates that the cumulative distribution of the near-grain
375 pore space is similar between the image-derived pore space and the HSIC geometry. In fact, 50%
376 of all pore space in both the porous media and HSIC model is approximately 20-25 μm from a
377 grain surface. Figure 3 (bottom) highlights that 25% of the entire pore space is further away from
378 the grain than expected by the HSIC geometry. The difference in maximum pore size between
379 Figure 2 (maximum radius of pore body ~160 μm) and Figure 3 (distance to nearest grain surface
380 ~180 μm) is due to the fact that no cropping was performed for Figure 3.

381

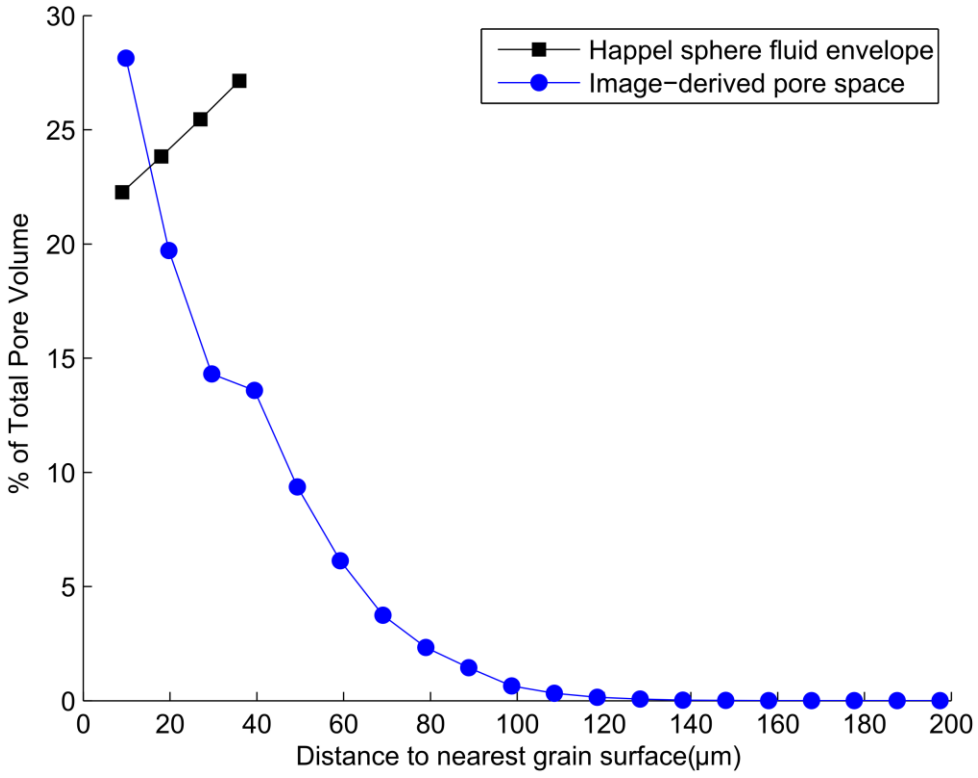

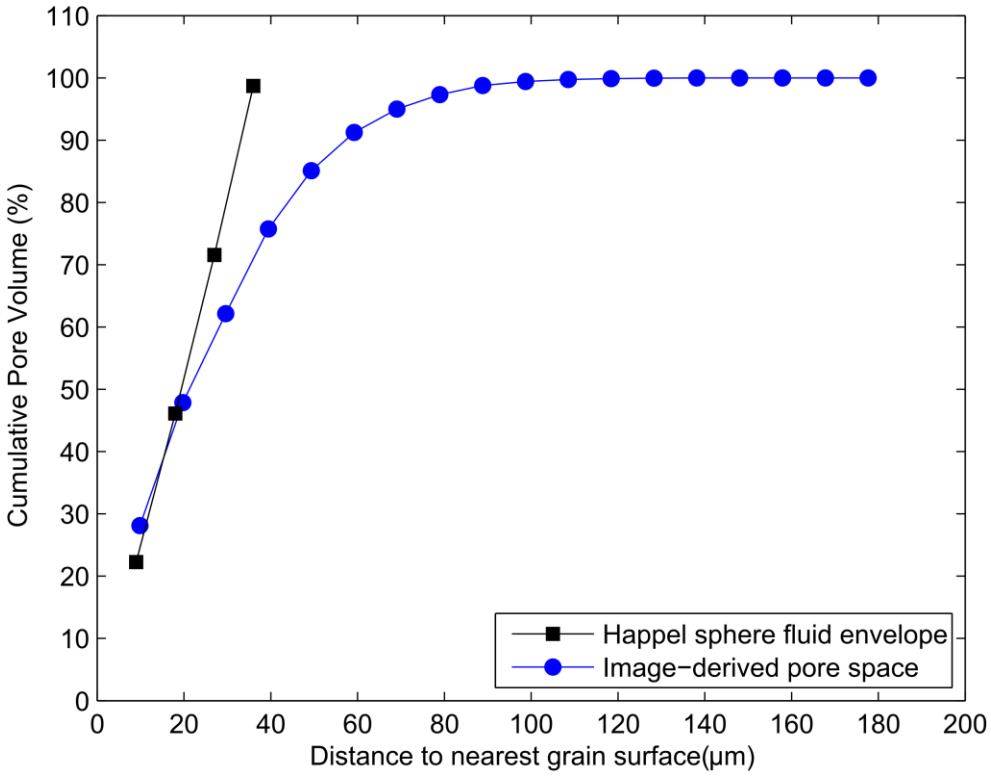

Figure 3 (top): The percentage of pore space as a function of distance from the nearest grain surface for the Happel sphere geometry (HSIC) (black squares) and the image-derived pore space (blue circle).

Figure 3 (bottom): The cumulative percentage of pore space as a function of distance from the nearest grain surface. Cumulative percentage refers to the sum of the geometries' pore space that is between the grain surface and a certain distance.

HSIC vs. SXCMT flow field

Averaging techniques were employed to analyze the CFD-simulated velocities in the image-derived pore space (see Figure 4 for a representative cross-section of velocity magnitude contours). The average pore water velocity around every grain in the image-derived pore space was plotted in Figure 4 (middle) as a function of distance from the nearest grain surface and angle from the downstream side of a grain (i.e. θ in Figure S2, measured from an axis parallel to the flow direction which passes through each grain's centroid). All voxels were sorted into 9.87 $\mu m \times 1^{o}$ bins and averaged to calculate an average velocity for every definable distance and angle bin around a grain. Therefore, the colour mapped in each bin represents the average velocity within the image-derived pore space at that particular distance and angle. For the analytical solution for flow through the HSIC model, a similar process was used, the analytical solution was solved in increments of 9.87 μm and 1º and a nearest neighbor interpolation routine was used to generate a radial surface plot (Figure 4, right). The white spaces at the center of the graphs are not meant to represent the collector surface, but appear because distances are measured between voxel centroids and cannot be smaller than half a voxel length (representing the distance from a voxel face to the closest voxel centroid).

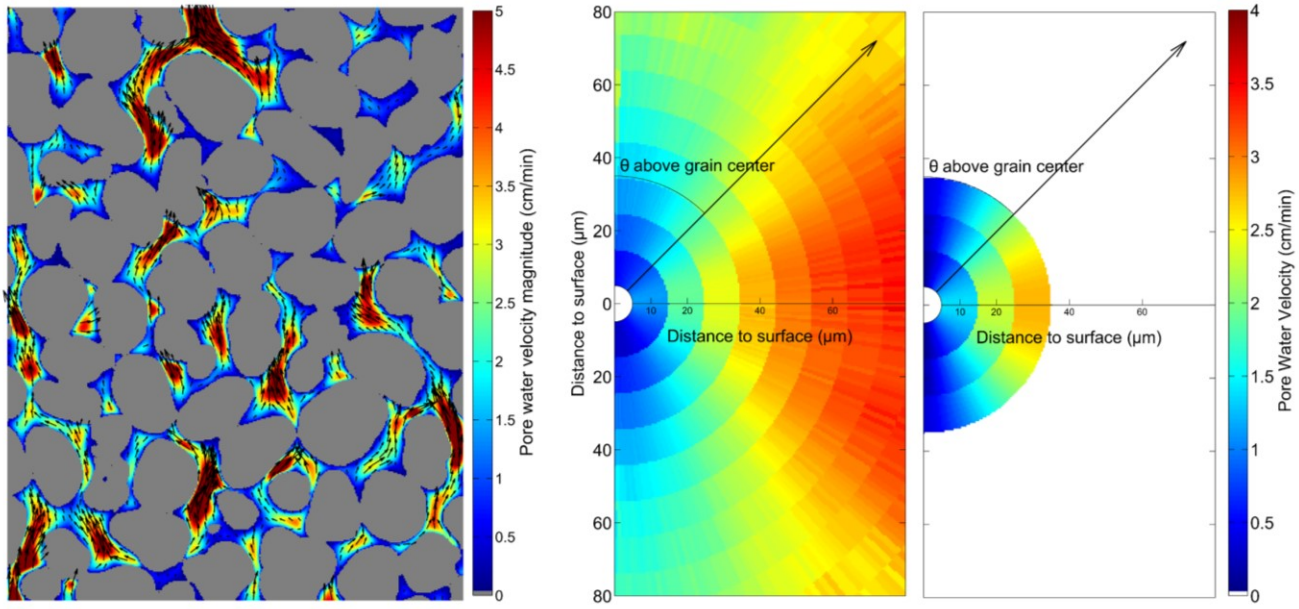

405
406 **Figure 4 left**: Contour plot of CFD-simulated pore water velocity magnitude overlain with black
407 streamlines from a representative image-derived pore space cross-section. The direction of flow is
408 upwards.
409 **Figure 4 middle**: Pore water velocity magnitude around the image-derived pore space. The direction of
410 flow is upwards. Further details on this figure are discussed in text.
411 **Figure 4 right**: Pore water velocity magnitude around the HSIC geometry (right). The direction of flow is
412 upwards. Further details on this figure are discussed in text.

413 The CFD-simulated flow field in the image-derived pore space illustrated in Figure 4 has
414 a number of important features. Average velocity in the image-derived pore space is observed to
415 be a function of angle with the highest velocities observed near the midpoint of the grain (θ =
416 90º) and relatively low velocity regions near the upstream (bottom) and downstream (top) sides
417 of the grain. The velocity distribution around the grain is also symmetric: the distribution on the
418 upstream and downstream sides of the grains are similar for all distances. This indicates that
419 there is little to no flow separation occurring on the downstream sides of the grains, which is
420 consistent with the typical definition of creeping flow. The average velocity increases with
421 distance from a grain surface with the highest velocities occurring in the centers of pores.

The flow field around the HSIC model (Figure 4, right) is in excellent qualitative agreement with the CFD-simulated flow field in the image-derived pore space (Figure 4, middle) within 36 μm of a grain's surface. The major velocity features in the image-derived pore space are captured by the HSIC flow field, including the relatively low-velocity regions on the upstream and downstream sides of the grains as well as the increase in velocity at $\theta = 90^{o}$ and the symmetric flow behavior. However, the HSIC model under-estimates velocities in the upstream and downstream regions (illustrated in Figure S3 and Figure 4); the velocities in the image-derived pore space at 0^{o} and 180^{o} near 20 μm are higher than the velocities in the HSIC fluid envelope. It is important to note that the above discussion compared the average flow velocity as a function of distance irrespective of pore size. It has been previously shown that a range of fluid velocities will occur even among similarly sized pores[65]. Thus the distribution of flow velocity at a certain distance from a grain surface may vary between pores based on factors such as pore connectivity, pore size, throat size and distribution of pore sizes [65]. The results in Figures 4 illustrate how these different flow distributions within each pore average out to yield a distribution that is similar to a simple analytical flow solution. However, previous studies have suggested that averaging flow fields in this manner may lose information vital to nanoparticle transport such as immobile zones in soil [8, 65] or preferential flow pathways in size distributed media[65].

To more quantitatively examine the distribution of velocities within the CFD-simulated image-derived pore space, Figure 5 plots the velocity distribution in Figure 4 as a one-dimensional function of distance to the nearest grain where the velocity was averaged over all angles for each particular distance interval with error bars representing the maximum and minimum values of velocity at each distance. Confirming the trend observed in Figure 4, the

445 average CFD-simulated and HSIC analytical velocities are very similar within the region
446 encompassed by the HSIC. Outside of the HSIC region, the average pore water velocities within
447 the centers of the largest pores (~100 μm) may be as large as 2× the overall average pore water
448 velocity (1.38 cm/min). This trend is qualitatively consistent with the velocity contour plot
449 illustrated in Figure 4 (left). Even within the HSIC region, the box and whisker plot in Figure 5
450 show that the individual values of CFD-simulated velocity can be upwards of 20 times larger
451 than within the HSIC model at identical distances from grain surfaces. Overall, these results
452 suggest that nanoparticles may be experiencing significantly higher fluid velocities than expected
453 within the CFT-HSIC model. These larger-than-expected velocities will yield forces and torques
454 on the nanoparticles that are outside the range considered by the CFT-HSIC mechanistic model.
455 To the best of the authors' knowledge this represents one of the first comparisons between CFD-
456 simulated velocities in a real sand and the HSIC model.

457

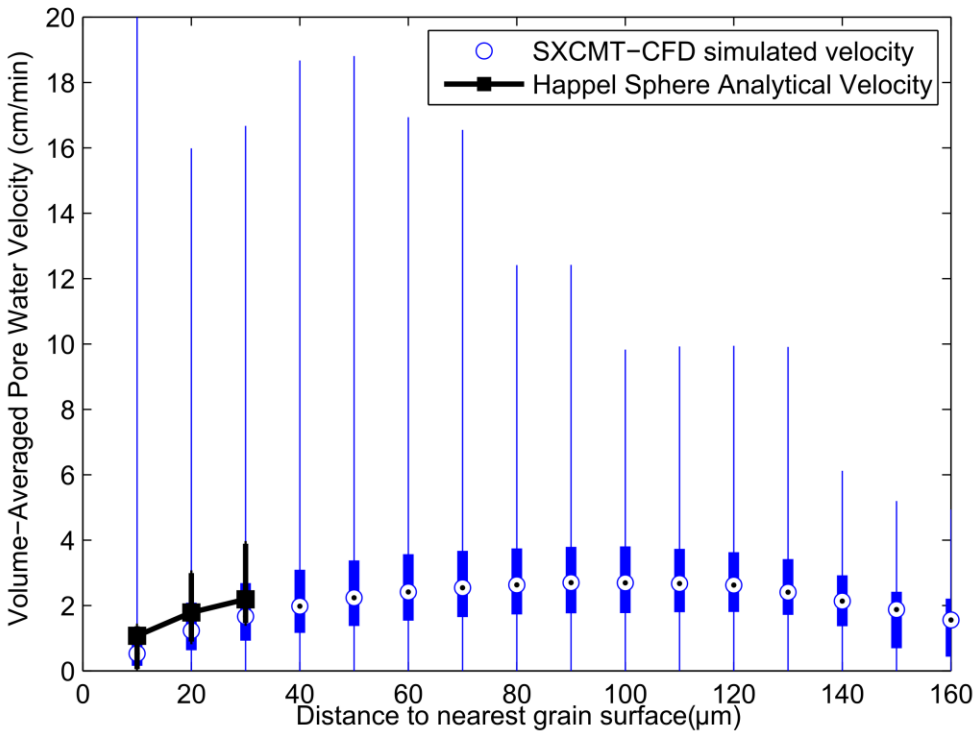

458

459 **Figure 5:** The average pore water velocity magnitude as a function of distance from the nearest grain
460 surface for both the HSIC geometry (black squares) and the image-derived pore space (blue circles with
461 a black dot). The velocity contours presented in Figure 4 were employed to create this plot; at each 9.87
462 μm distance interval the velocities were averaged over all 1° bins (i.e., each datapoint represents
463 velocity averaged over 0 – 180 °) and weighted by the fraction of pore volume in each 1 ° bin. The
464 SXCMT-CFD simulated velocity distribution is presented as a box-and-whisker plot where the bounds of
465 the boxes represent the 25% and 75% quartile at each distance and the length of the whiskers
466 represents the minimum and maximum velocity at each distance. The error bars on the Happel Sphere
467 Analytical Velocity profile represents the maximum and minimum velocities at each distance from the
468 grain surface.

469

470

471

472

Nanoparticle mass distribution in qSXCMT datasets

Figure 6 presents the distribution of nanoparticle mass within the qSXCMT dataset as a function of distance to the nearest grain surface for each imaged time-step. The mass distribution curves were calculated by first determining the nanoparticle mass in each voxel, calculated by multiplying each voxel's qSXCMT-determined concentration by the volume of the voxel (approximately 961.5 μm^3). This calculation was repeated for every voxel > 17.3µm from a grain surface (i.e., outside the shadow zone). The distance between every pore space voxel and the nearest grain surface in each qSXCMT dataset was measured and sorted into 9.87 µm intervals. The nanoparticle mass in each interval was plotted as a function of mass versus distance to the nearest surface (Figure 6, top).

As illustrated in Figure 6 (top), most nanoparticle mass is located near the grain surface; this is expected as the near surface regions possess the largest volume of pore space (shown in Figure 3). While the qSXCMT method is currently unable to quantify nanoparticle mass closer than 17.3 µm (25% of the total pore space, Figure 3), based on the trend in Figure 3, it is hypothesized that, in general, the total mass of nanoparticles continues increasing with decreasing distance to the grain surface. The term 'quantifiable mass' is used throughout this section to refer to mass, or mass flow, outside of the 'shadow zone' that can be quantified via the qSXCMT procedure.

The general shape of the mass distribution curve in Figure 6 (top) approximates the shape of the pore space volume curve in Figure 3 (top). To quantitatively compare the distributions of mass and volume, Figure 6 (bottom) plots the cumulative percentage of quantifiable nanoparticle mass as a function of distance to the nearest grain surface. This represents the total percentage of

quantifiable nanoparticle mass that is closer to the grain surface than a certain distance. Figure 6 suggests that, at every time-step, only approximately 60% of all quantifiable nanoparticle mass is within the fluid region encompassed by the HSIC fluid envelope.

Figure 3 can be employed to estimate the nanoparticle mass distribution in the 'shadow zone' region, which accounts for 25% of all pore space voxels. Assuming a strictly per-volume ratio, 75% of the total nanoparticle mass can be quantified via qSXCMT at each time step. Incorporating this into the cumulative percentages in Figure 6 (bottom) yields an adjusted estimate of approximately 70% of total nanoparticle mass within the HSIC fluid envelope region with 30% of nanoparticle mass outside of the envelope. The percentage of nanoparticle mass outside the envelope is greater than the percentage of pore volume outside the envelope. This indicates that nanoparticles are not uniformly distributed throughout the pore space and that the pore-scale concentration gradients identified by Molnar et al. [8] significantly affect the overall mass distribution through the pore space. It should be noted that while this distribution is for nanoparticle mass in an 'unfavorable' deposition scenario, a previous study conducted on this same dataset concluded that the presence of a repulsive energy barrier had no observable impact on the pore-scale distribution of nanoparticle concentration at the scale examined in Figure 6[8].

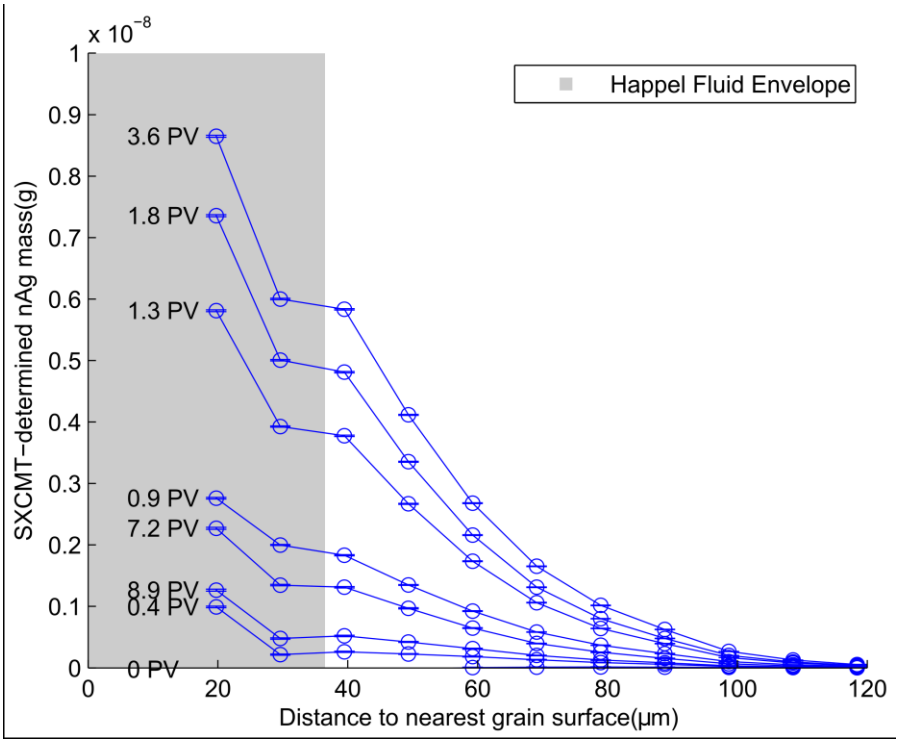
x 10^-8
SXCMT-determined nAg mass(g)
Distance to nearest grain surface(μm)
Happel Fluid Envelope
3.6 PV
1.8 PV
1.3 PV
0.9 PV
7.2 PV
8.9 PV
0.4 PV
0 PV

512

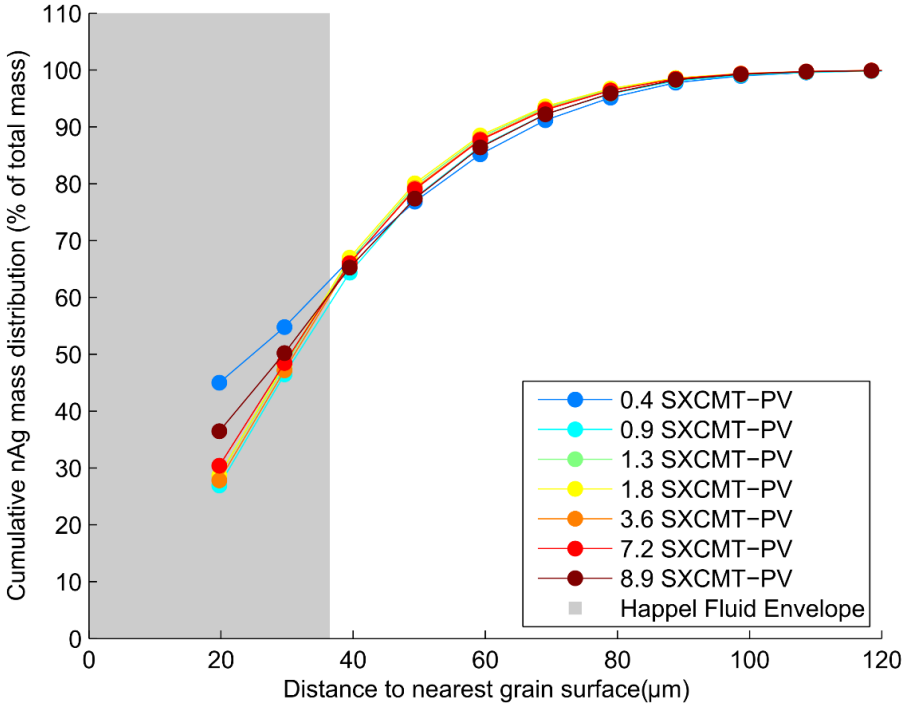
Cumulative nAg mass distribution (% of total mass)
Distance to nearest grain surface(μm)
0.4 SXCMT-PV
0.9 SXCMT-PV
1.3 SXCMT-PV
1.8 SXCMT-PV
3.6 SXCMT-PV
7.2 SXCMT-PV
8.9 SXCMT-PV
Happel Fluid Envelope

513

514

515 **Figure 6 (top)**: The qSXCMT-determined nAg mass plotted as a function of distance from the nearest
516 grain surface (top) for each imaged time-step. The gray box represents the thickness *r* of the HSIC fluid
517 envelope. To avoid cluttering the figure, 'PV' is used instead of 'SXCMT-PV's'. The error bars on the
518 qSXCMT dataset lines represent 95% confidence intervals calculated at each datapoint. Every datapoint
519 in the qSXCMT dataset has an error bar, however the error bars may be smaller than the size of the data
520 point marker and not visible.

521 **Figure 6 (bottom):** The cumulative percentage of qSXCMT-determined nAg mass for each imaged time-
522 step as a function of distance from the nearest grain surface. Cumulative percentage refers to the total
523 percentage of nAg mass that is between the grain surface and a certain distance from the surface.

524 The 1-dimensional (1-D) CFD flow field and the 1-D distribution of nanoparticle mass
525 were combined to estimate the 1-D averaged nanoparticle advective mass *flux* rates (mass flow
526 of nAg per unit area). This analysis was conducted to develop an understanding of how close
527 advective flow through a realistic 3-dimensional porous media domain will bring nanoparticles
528 to a collector surface, as such no diffusive flux was considered in this analysis. Calculations of
529 the maximum possible change in concentration due to diffusive flux indicates that diffusive flux
530 is negligible compared to the estimated advective flux rates. The estimated 1-D nanoparticle
531 mass *flux* are plotted as a function of distance to the nearest grain surface. The 1-D
532 concentration distribution was calculated by dividing the mass distribution in Figure 6 by the
533 distribution of pore space in Figure 3, which yields an average concentration value for each
534 binned distance from a grain surface. The 1-D CFD velocity magnitude plot in Figure 5 was
535 separated into its component velocities (v_x, v_y and v_z), each of these 1-D distributions of
536 component velocities was multiplied by the 1-D concentration distribution to estimate mass *flux*
537 distributions in the x, y and z directions (q_x, q_y and q_z). These component mass *flux* distributions
538 were summed to determine an overall mass *flux* distribution ($q = q_x + q_y + q_z$) as a function of
539 distance to the nearest grain surface. This mass *flux* distribution is illustrated in the supporting
540 material (Figure S4).

Due to the high velocities and higher concentrations in the centers of the larger pores, mass *flux* rates were the highest at the centers of the pores for the time-steps between 0.9 and 3.6 SXCMT-PV's and, to a lesser extent, 7.2 SXCMT-PV. The mass *flux* rates do not appreciably change with distance from the grain surface for the early time-step 0.4 SXCMT-PV and the last time-step 8.9 SXCMT-PV; this is likely due to the minimal concentration gradients noted by Molnar et al. [8] at these times.

The average mass *flux* distributions were employed to estimate the total quantifiable nanoparticle mass flow rate distribution. Component mass flow rates in the x, y and z directions (Q_x, Q_y and Q_z) were estimated by multiplying the distribution of component mass *flux* rates (q_x, q_y and q_z) by the number of voxels within each 9.87 μm distance interval and by the area of a voxel face (9.87×9.87 μm). The component mass flow rates were then summed to yield the nanoparticle mass flow rate distribution ($Q = Q_x + Q_y + Q_z$) in Figure 7.

Figure 7 (top) represents the quantifiable mass flow as a function of distance from the grain surface and is qualitatively different from the distribution of pore space. The nanoparticle mass flow rate exhibits a bi-modal distribution with one peak near the grain surface and a second peak at a distance of 40 μm. The location of this second peak mass flow rate was unexpected as it does not occur at a region of peak nanoparticle mass, mass *flux* or fluid velocity. This second peak is likely due to a combination of several factors including nanoparticle concentration distribution, fluid velocity distribution, the distribution of small, medium and large pores illustrated in Figure 2 and the overall distribution of pore space illustrated in Figure 3. This bi-modal peak is not attributed to the presence of a repulsive energy barrier as it was previously shown that unfavorable conditions do not impact the distribution of pore-scale nanoparticle concentrations at the scales examined here[8].

564 Figure 7 (bottom) plots the cumulative percentage of quantifiable nanoparticle mass flow
565 as a function of distance to the nearest grain surface. The cumulative percentage at the edge of
566 the HSIC fluid envelope can be used to compare the distributions of pore space volume,
567 nanoparticle mass and mass flow. Accounting for the pore space volume within the 'shadow
568 zone' in the same manner as the mass distribution (Figure 6) discussed above, approximately
569 37% of total nanoparticle mass flow is occurring further away from the grain surface than
570 considered by the HSIC model. Moreover, more mass flow is occurring further away from the
571 grain surface than would be expected by either the proportion of pore space (25%) or
572 nanoparticle mass (30%) outside of the envelope. The distribution of velocity in Figure 5 is
573 responsible for the mass flow that favours the centers of pores.

574

575

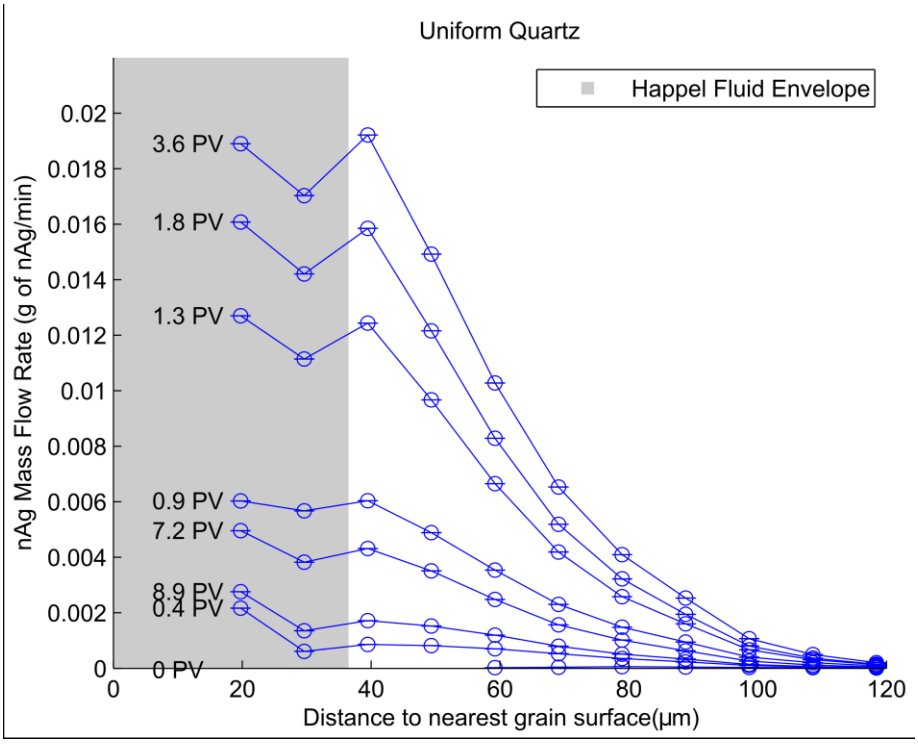

576

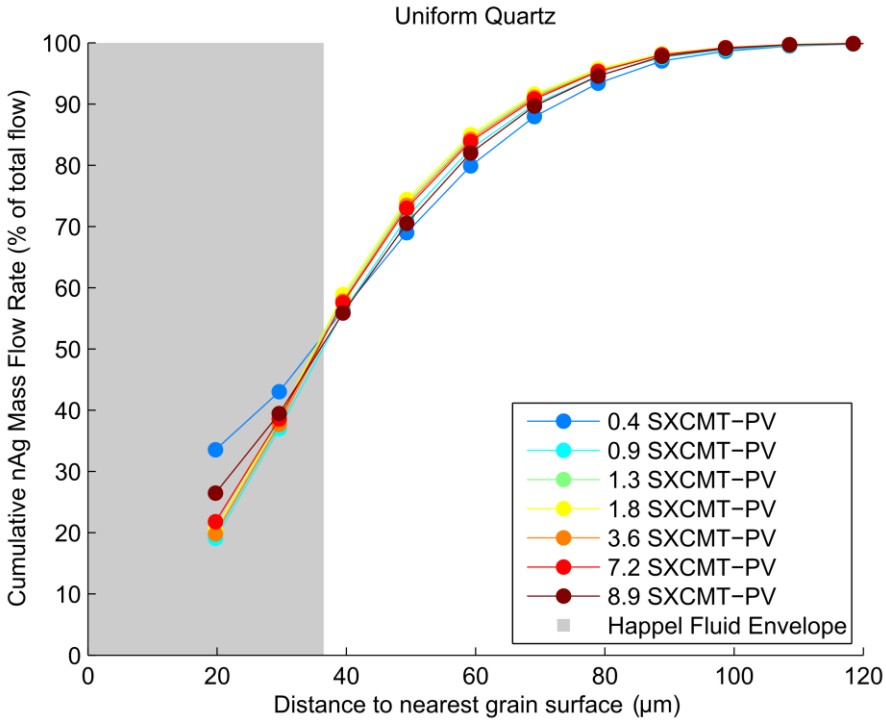

Figure 7 (top): The estimated nAg mass flow rate as a function of distance from the nearest grain surface for each imaged time-step. The gray box represents the thickness *r* of the HSIC fluid envelope. To avoid cluttering the figure, 'PV' is used instead of 'SXCMT-PV's'.

Figure 7 (bottom): The cumulative percentage of estimated nAg nanoparticle mass flow for each imaged time-step as a function of distance from the nearest grain surface. Cumulative percentage refers to the total percentage of nAg mass flow occurring between the grain surface and a certain distance from the surface.

Discussion

These results indicate that the HSIC geometry results in a 'compression' of the actual pore space; it is hypothesized that this may be impacting the accuracy of CFT-HSIC's predictions for nanoparticle transport. The trends in pore size and pore space highlighted in Figures 4 and 5 suggest that the HSIC model, purely on the basis of pore geometry, will treat flow and transport processes as being closer to the grain surface than they would be within medium-to-larger pores in the qSXCMT dataset. Thus flow and transport processes such as the

diffusive flux of nanoparticles towards a grain surface, which could be occurring upwards of 197 μm away, the maximum distance from a grain surface identified within the qSXCMT datasets, will be treated by HSIC as being within 36 μm of a grain surface. Approximately 80% of all uniquely identified pore bodies are affected by this pore space compression, and 25% of the total pore space in the qSXCMT-dataset is treated by the HSIC geometry as being closer to a grain surface than it actually is. Given the similarities in grain shape between this study and a previous study [64], this trend is likely widely present in sandy media.

Figures 6 and 7 indicate that large percentages of nanoparticle mass (30%) and mass flow (37%) are further away from the grain surface than is considered by the HSIC model. These percentages remain consistent for all time-steps through the transport experiment. The degree to which CFT's prediction of colloid retention is affected by these percentages depends on the process governing colloid transport. Micron-sized colloids rely on interception (commonly denoted by η_I) to contact the grain surface e.g. [36, 37]. Interception is when colloids are flowing along a streamline which passes within 1 colloid radius of the collector surface and contact the surface by virtue of their size. The micron-sized colloids exhibit a minimal degree of Brownian motion – diffusion of particles arising from collisions with surrounding molecules – and are not expected to diffuse across a significant number of streamlines. This strong interception behavior, coupled with weak diffusive transport, suggests that in the absence of gravitational settling only colloids on specific trajectories will be contacting and attaching to the collector; the 'critical trajectory' refers to the trajectory beyond which colloids will no longer intercept the grain surface. Rajagopalan and Tien [37] employ this concept to simplify their calculations by only considering colloids within the critical trajectory. As a result, the accuracy of CFT for micron-size colloid transport and retention will depend on how well the modeled geometry captures the

616 streamlines within a realistic medium. Geometry simplifications will adversely impact the
617 accuracy of streamlines within CFT models. However, the good agreement between the
618 analytical HSIC and CFD-simulated flow fields (Figure 4) suggests that, on average, the near-
619 surface flow field through the image derived pore space (<36 μm from a collector surface) is
620 approximated reasonably well by the HSIC model. This result, in combination with the strong
621 interception and weak diffusive behaviour of micron-sized colloids, suggests that this geometry
622 can be appropriate for predicting micron-sized colloid retention rates. This may be a reason for
623 why micron-sized particle behaviour has been shown to be accurately modelled by CFT-HSIC
624 models[38], however trajectory simulations of micron-sized colloids are needed to confirm this
625 hypothesis.

626 However, interception is not a dominant mechanism for nanoparticles. Due to
627 nanoparticles' small radii there are only a small number of trajectories which will bring
628 nanoparticles within 1 colloid radius of the collector. For nanoparticles, diffusion is the main
629 mechanism for contacting collector surfaces (commonly denoted by η_D)[46]. The fraction of
630 nanoparticles diffusing distances of 0 – 36 μm across the HSIC envelope will be much larger
631 than in the porous medium where diffusive distance can range from 0 – 197 μm (the maximum
632 distance from a grain surface in the image-derived pore space) . Given these results showing a
633 substantial mass flow of nanoparticles is further away from the grain surface than expected by
634 HSIC, approximating all nanoparticles as being within the 36μm HSIC envelope is expected to
635 cause the model to over-estimate η and nanoparticle retention rates. This is hypothesized to be a
636 reason that HSIC-CFT models typically over-predict η and k_{att} [8, 38, 46].

637 The results presented in Figure 2, 5, 6 and 7 suggest that nanoparticle transport studies
638 which employ η-correlation equations from CFT to estimate η e.g., [24, 25, 26, 27, 28, 29, 30, 31, 32, 33, 34, 35]

639 are over-predicting η due to the CFT-HSIC geometry's inability to consider nanoparticle mass
640 flow outside the fluid envelope. It should be noted that, as this study does not employ a
641 mechanistic particle tracking model for trajectory analysis, the proposed link between
642 nanoparticle mass flow outside the Happel envelope and CFT over-prediction remains a
643 hypothesis and should be considered an open research question. CFT models are starting to
644 employ alternative geometries such as the Hemisphere-in-Cell model [66], cylindrical pore model[67]
645 and the randomly packed collector model [46, 68], however it is unknown if these geometries will
646 overcome the limitations of the HSIC geometry in predicting nanoparticle retention. Many of
647 these alternative geometries are highly tunable and, as such, are promising potential avenues for
648 trajectory analysis and exploring the link between compressed pore space and CFT over-
649 prediction of nanoparticle attachment.

650 For nanoparticle transport, it is expected that the accuracy of a mechanistic CFT model is
651 linked to how well its geometry mimics the distribution of pore space, and the range of diffusive
652 distances required to reach a grain surface, found in realistic porous media. Nelson and Ginn [38]
653 examined this link; they compared the relative accuracy of 5 different mechanistic CFT models
654 with different geometries of which 3 employed the HSIC[37, 38, 40], 1 employed a random sphere
655 packing[46], 1 employed a 'Hemisphere-in-Cell' model [41, 43, 69, 70, 71]. While their results suggested
656 no observable correlation between geometry realism and accuracy, the 5 models incorporated
657 different flow fields, force-torque balances and different treatments of Brownian motion [4] which
658 makes it impossible to compare the accuracy of those models solely on the basis of geometry.
659 Further study is required to examine the link between geometry realism and model accuracy. Of
660 note is the 'Hemisphere-in-Cell' model which includes concentric fluid envelopes around each
661 hemisphere in a manner similar to the HSIC model, but also incorporates a simplified force

662 balance for colloids outside of the fluid envelope [70] and a pendular ring [43] for the express purpose
663 of adding a small volume of pore space at slightly further distances from the grain surface. While
664 these additions are unlikely to encapsulate the full range of diffusive distances observed in
665 Figure 7, they do bring a degree of increased realism to a unit-cell model and could thereby
666 potentially improve predictions for nanoparticle attachment.

667 In favorable DLVO conditions where $\alpha = 1$ (i.e., attachment efficiency = 1) this over-
668 prediction of η will result in over-predictions of the nanoparticle kinetic retention rate coefficient
669 k_{att} and over-predictions of the overall rate of nanoparticle retention. This may result in under-
670 predictions of nanoparticle mobility and risk to nearby drinking water supplies. In unfavorable
671 DLVO conditions where $\alpha < 1$, a-priori estimations of η are required to accurately determine α.
672 CFT-HSIC over-predictions of η will then result in under-estimations of α. Numerous studies
673 have tried to identify trends in nanoparticle α [1, 29, 32, 72, 73, 74, 75] but with generally limited success.
674 This limited success in describing α for nanoparticle transport may be due, in part, to the
675 inability to accurately predict η with CFT-HSIC mechanistic models and correlation equations.

676 The pore-scale distribution and behavior of nanoparticles within real porous media is
677 currently poorly understood [4], so it is unclear the degree to which the extended diffusive
678 distances (0–36 μm vs 0–197 μm) contribute to over-predicted retention rates as opposed to other
679 proposed mechanisms (e.g., immobile zones) [8]. Further research is required to determine how
680 fluid and nanoparticle parameters (e.g., particle size, viscosity), as well as different types of
681 porous media (e.g., geometry, surface properties) influence the 'diffusive error' arising from
682 compressing larger pore bodies into thin HSIC fluid envelopes.

683 # Summary and Conclusions

Pore-scale silver nanoparticle distributions were imaged via quantitative Synchrotron X-ray Computed MicroTomography (qSXCMT) and linked with Computational Fluid Dynamics simulations of fluid flow through the imaged pore space. This examination yielded some of the first ever quantitative evaluation of pore-scale nanoparticle transport through a real porous medium. Summarized findings include: (1) The pore space ranged from 0 – 197 μm from a grain surface, of which 25% was further from the grain than the 36 μm fluid envelope assumed by the HSIC model; (2) Average pore velocity, which is a function of distance from the grain surface, agreed well between the experiment and HSIC model within the HSIC fluid envelope; however, the former were 2 times larger than the latter in the centers of the larger pores; (3) The individual values of CFD-simulated velocity were upwards of 20 times those of the HSIC model at identical distances from grain surfaces; and (4) Approximately 30% of all nanoparticle mass and 37% of all nanoparticle mass flow occur further away from the grain surface than expected by the HSIC geometry. While it is generally widely acknowledged that the Happel Sphere model is a simplification of real porous media systems, this paper is one of the first studies that provides a detailed examination of which components of real porous media are simplified specifically with respect to nanoparticle transport. Overall, this work suggests that the HSIC geometry assumptions are unnaturally compressing the pore space around the Happel sphere. It is therefore hypothesized that a significantly lower fraction of nanoparticles will contact a grain surface by diffusion than expected by HSIC geometry. Moreover, it is hypothesized that this difference between reality and model, termed 'diffusive error', is likely contributing to CFT-HSIC's typical over-predictions of η for nanoparticles. This study also confirms that, despite these simplifications, the average pore space distribution and the average velocity distribution within 36μm of a grain surface are well represented by the HSIC geometry.

We acknowledge that we only examined nanoparticle transport through one soil sample (a relatively uniform quartz sand), so the results from this study – such as the percentages of nanoparticles outside the HSIC fluid envelope –are specific to the grain and pore distribution in the examined qSXCMT datasets as well as the experimental fluid velocity. In addition, this study only examined unfavorable conditions. However, these results are not expected to be sensitive to grain surface chemistry/DLVO interactions as the distances examined within this study are orders of magnitude larger than the scale at which DLVO interactions are significant. In addition, Molnar et al. [8] noted that the concentration gradients within a pore did not change between unfavorable and favorable deposition conditions. These limitations do not alter the findings of this study, that a significant fraction of nanoparticles are further away from the grain surface than considered by standard CFT models. It should be noted that the implications of this finding, a proposed link between the compressed pore space in HSIC and over-prediction of nanoparticle attachment by CFT, remains a hypothesis and should be considered a valuable avenue for future research. Future work on this topic should include modifying existing CFT geometries such as the HSIC or Hemisphere geometry, or developing new geometries, and employing trajectory analysis with a mechanistic model to further evaluate the hypothesis and quantify the impact of the compressed pore space on CFT predictions of collector efficiency . In addition, future work should pay specific attention to developing CFT geometries and models that are appropriate for nanoparticle transport and consider the full range of pore sizes that are present. Future work on this topic should also examine the results presented in this study for a range of porous media and nanoparticle types. Research on nanoparticle-specific CFT geometries has begun (see [46, 68]) and further developing these models and concepts should be considered a promising avenue of research.

Acknowledgements

We acknowledge the support of GeoSoilEnviroCARS (Sector 13), which is supported by the National Science Foundation - Earth Sciences (EAR-1128799), and the Department of Energy, Geosciences (DE-FG02-94ER14466). Use of the Advanced Photon Source, an Office of Science User Facility operated for the U.S. Department of Energy (DOE) Office of Science by Argonne National Laboratory, was supported by the U.S. DOE under Contract No. DE-AC02-06CH11357. This research was supported by the Natural Sciences and Engineering Research Council (NSERC) of Canada. Portions of this research (CFD simulations) were conducted with high performance computing resources provided by Louisiana State University (http://www.hpc.lsu.edu).

References

1. Petosa, A. R.; Jaisi, D. P.; Quevedo, I. R.; Elimelech, M.; Tufenkji, N. Aggregation and Deposition of Engineered Nanomaterials in Aquatic Environments: Role of Physicochemical Interactions. *Environ. Sci. Technol.* **2010,** *44* (17), 6532-6549.
2. O'Carroll, D.; Sleep, B.; Krol, M.; Boparai, H.; Kocur, C. Nanoscale zero valent iron and bimetallic particles for contaminated site remediation. *Adv. Water Resour.* **2013,** *51* (0), 104-122.
3. Goldberg, E.; Scheringer, M.; Bucheli, T. D.; Hungerbühler, K. Critical Assessment of Models for Transport of Engineered Nanoparticles in Saturated Porous Media. *Environ. Sci. Technol.* **2014,** *48* (21), 12732-12741.
4. Molnar, I. L.; Johnson, W. P.; Gerhard, J. I.; Willson, C. S.; O'Carroll, D. M. Predicting colloid transport through saturated porous media: A critical review *Water Resour. Res.* **2015,** *51* (50th anniversary special collection), 6804-6845.
5. Jiang, X.; Tong, M.; Kim, H. Influence of natural organic matter on the transport and deposition of zinc oxide nanoparticles in saturated porous media. *Journal of Colloid and Interface Science* **2012,** *386* (1), 34-43.
6. Jiang, X.; Tong, M.; Lu, R.; Kim, H. Transport and deposition of ZnO nanoparticles in saturated porous media. *Colloids and Surfaces A: Physicochemical and Engineering Aspects* **2012,** *401* (0), 29-37.
7. Uyusur, B.; Darnault, C. J. G.; Snee, P. T.; Koken, E.; Jacobson, A. R.; Wells, R. R. Coupled effects of solution chemistry and hydrodynamics on the mobility and transport of quantum dot nanomaterials in the vadose zone. *Journal of Contaminant Hydrology* **2010,** *118* (3-4), 184-198.

8. Molnar, I. L.; Gerhard, J. I.; Willson, C. S.; O'Carroll, D. M. The impact of immobile zones on the transport and retention of nanoparticles in porous media. *Water Resour. Res.* **2015**.
9. Kanel, S.; Flory, J.; Meyerhoefer, A.; Fraley, J.; Sizemore, I.; Goltz, M. Influence of natural organic matter on fate and transport of silver nanoparticles in saturated porous media: laboratory experiments and modeling. *J. Nanopart. Res.* **2015,** *17* (3), 1-13.
10. Joo, S. H.; Al-Abed, S. R.; Luxton, T. Influence of Carboxymethyl Cellulose for the Transport of Titanium Dioxide Nanoparticles in Clean Silica and Mineral-Coated Sands. *Environ. Sci. Technol.* **2009,** *43* (13), 4954-4959.
11. Lanphere, J. D.; Luth, C. J.; Walker, S. L. Effects of Solution Chemistry on the Transport of Graphene Oxide in Saturated Porous Media. *Environ. Sci. Technol.* **2013,** *47* (9), 4255-4261.
12. Liang, Y.; Bradford, S. A.; Simunek, J.; Vereecken, H.; Klumpp, E. Sensitivity of the transport and retention of stabilized silver nanoparticles to physicochemical factors. *Water Research* **2013,** *47* (7), 2572-2582.
13. Liang, Y.; Bradford, S. A.; Simunek, J.; Heggen, M.; Vereecken, H.; Klumpp, E. Retention and Remobilization of Stabilized Silver Nanoparticles in an Undisturbed Loamy Sand Soil. *Environ. Sci. Technol.* **2013,** *47* (21), 12229-12237.
14. Wang, D.; Ge, L.; He, J.; Zhang, W.; Jaisi, D. P.; Zhou, D. Hyperexponential and nonmonotonic retention of polyvinylpyrrolidone-coated silver nanoparticles in an Ultisol. *Journal of Contaminant Hydrology* **2014,** *164* (0), 35-48.
15. Wang, Y.; Li, Y.; Costanza, J.; Abriola, L. M.; Pennell, K. D. Enhanced Mobility of Fullerene (C60) Nanoparticles in the Presence of Stabilizing Agents. *Environ. Sci. Technol.* **2012,** *46* (21), 11761-11769.
16. Wang, Y.; Li, Y.; Fortner, J. D.; Hughes, J. B.; Abriola, L. M.; Pennell, K. D. Transport and Retention of Nanoscale C60 Aggregates in Water-Saturated Porous Media. *Environ. Sci. Technol.* **2008,** *42* (10), 3588-3594.
17. Wang, D.; Zhang, W.; Zhou, D. Antagonistic Effects of Humic Acid and Iron Oxyhydroxide Grain-Coating on Biochar Nanoparticle Transport in Saturated Sand. *Environ. Sci. Technol.* **2013,** *47* (10), 5154-5161.
18. Wang, D.; Zhang, W.; Hao, X.; Zhou, D. Transport of Biochar Particles in Saturated Granular Media: Effects of Pyrolysis Temperature and Particle Size. *Environ. Sci. Technol.* **2013,** *47* (2), 821-828.
19. Kasel, D.; Bradford, S. A.; Šimůnek, J.; Heggen, M.; Vereecken, H.; Klumpp, E. Transport and retention of multi-walled carbon nanotubes in saturated porous media: Effects of input concentration and grain size. *Water Research* **2013,** *47* (2), 933-944.
20. Wang, Y.; Becker, M. D.; Colvin, V. L.; Abriola, L. M.; Pennell, K. D. Influence of Residual Polymer on Nanoparticle Deposition in Porous Media. *Environ. Sci. Technol.* **2014,** *48* (18), 10664-10671.
21. Li, Y.; Wang, Y.; Pennell, K. D.; Abriola, L. M. Investigation of the Transport and Deposition of Fullerene (C60) Nanoparticles in Quartz Sands under Varying Flow Conditions. *Environ. Sci. Technol.* **2008,** *42* (19), 7174-7180.
22. Solovitch, N.; Labille, J.; Rose, J.; Chaurand, P.; Borschneck, D.; Wiesner, M. R.; Bottero, J.-Y. Concurrent Aggregation and Deposition of TiO2 Nanoparticles in a Sandy Porous Media. *Environ. Sci. Technol.* **2010,** *44* (13), 4897-4902.
23. Chen, G.; Liu, X.; Su, C. Transport and Retention of TiO2 Rutile Nanoparticles in Saturated Porous Media under Low-Ionic-Strength Conditions: Measurements and Mechanisms. *Langmuir* **2011,** *27* (9), 5393-5402.
24. Krol, M. M.; Oleniuk, A. J.; Kocur, C. M.; Sleep, B. E.; Bennett, P.; Xiong, Z.; O'Carroll, D. M. A Field-Validated Model for In Situ Transport of Polymer-Stabilized nZVI and Implications for Subsurface Injection. *Environ. Sci. Technol.* **2013,** *47* (13), 7332-7340.

25. Mattison, N. T.; O'Carroll, D. M.; Kerry Rowe, R.; Petersen, E. J. Impact of Porous Media Grain Size on the Transport of Multi-walled Carbon Nanotubes. *Environ. Sci. Technol.* **2011,** *45* (22), 9765-9775.

26. Liu, X. Y.; O'Carroll, D. M.; Petersen, E. J.; Huang, Q. G.; Anderson, C. L. Mobility of Multiwalled Carbon Nanotubes in Porous Media. *Environ. Sci. Technol.* **2009,** *43* (21), 8153-8158.

27. Taghavy, A.; Mittelman, A.; Wang, Y.; Pennell, K. D.; Abriola, L. M. Mathematical Modeling of the Transport and Dissolution of Citrate-Stabilized Silver Nanoparticles in Porous Media. *Environ. Sci. Technol.* **2013,** *47* (15), 8499-8507.

28. Lecoanet, H. F.; Bottero, J.-Y.; Wiesner, M. R. Laboratory Assessment of the Mobility of Nanomaterials in Porous Media. *Environ. Sci. Technol.* **2004,** *38* (19), 5164-5169.

29. Tong, M.; Johnson, W. P. Excess Colloid Retention in Porous Media as a Function of Colloid Size, Fluid Velocity, and Grain Angularity. *Environ. Sci. Technol.* **2006,** *40* (24), 7725-7731.

30. Jaisi, D. P.; Elimelech, M. Single-Walled Carbon Nanotubes Exhibit Limited Transport in Soil Columns. *Environ. Sci. Technol.* **2009,** *43* (24), 9161-9166.

31. El Badawy, A. M.; Aly Hassan, A.; Scheckel, K. G.; Suidan, M. T.; Tolaymat, T. M. Key Factors Controlling the Transport of Silver Nanoparticles in Porous Media. *Environ. Sci. Technol.* **2013**.

32. Lin, S. H.; Cheng, Y. W.; Bobcombe, Y.; Jones, K. L.; Liu, J.; Wiesner, M. R. Deposition of Silver Nanoparticles in Geochemically Heterogeneous Porous Media: Predicting Affinity from Surface Composition Analysis. *Environ. Sci. Technol.* **2011,** *45* (12), 5209-5215.

33. Ryan, J. N.; Harvey, R. W.; Metge, D.; Elimelech, M.; Navigato, T.; Pieper, A. P. Field and Laboratory Investigations of Inactivation of Viruses (PRD1 and MS2) Attached to Iron Oxide-Coated Quartz Sand. *Environ. Sci. Technol.* **2002,** *36* (11), 2403-2413.

34. Phenrat, T.; Kim, H. J.; Fagerlund, F.; Illangasekare, T.; Lowry, G. V. Empirical correlations to estimate agglomerate size and deposition during injection of a polyelectrolyte-modified Fe-0 nanoparticle at high particle concentration in saturated sand. *Journal of Contaminant Hydrology* **2010,** *118* (3-4), 152-164.

35. Phenrat, T.; Song, J. E.; Cisneros, C. M.; Schoenfelder, D. P.; Tilton, R. D.; Lowry, G. V. Estimating Attachment of Nano- and Submicrometer-particles Coated with Organic Macromolecules in Porous Media: Development of an Empirical Model. *Environ. Sci. Technol.* **2010,** *44* (12), 4531-4538.

36. Yao, K.-M.; Habibian, M. T.; O'Melia, C. R. Water and waste water filtration. Concepts and applications. *Environ. Sci. Technol.* **1971,** *5* (11), 1105-1112.

37. Rajagopalan, R.; Tien, C. TRAJECTORY ANALYSIS OF DEEP-BED FILTRATION WITH SPHERE-IN-CELL POROUS-MEDIA MODEL. *Aiche J.* **1976,** *22* (3), 523-533.

38. Nelson, K. E.; Ginn, T. R. New collector efficiency equation for colloid filtration in both natural and engineered flow conditions. *Water Resour. Res.* **2011,** *47*, 17.

39. Cushing, R. S.; Lawler, D. F. Depth Filtration: Fundamental Investigation through Three-Dimensional Trajectory Analysis. *Environ. Sci. Technol.* **1998,** *32* (23), 3793-3801.

40. Tufenkji, N.; Elimelech, M. Correlation equation for predicting single-collector efficiency in physicochemical filtration in saturated porous media. *Environ. Sci. Technol.* **2004,** *38* (2), 529-536.

41. Ma, H.; Pedel, J.; Fife, P.; Johnson, W. P. Hemispheres-in-Cell Geometry to Predict Colloid Deposition in Porous Media. *Environ. Sci. Technol.* **2009,** *43* (22), 8573-8579.

42. Messina, F.; Marchisio, D. L.; Sethi, R. An extended and total flux normalized correlation equation for predicting single-collector efficiency. *Journal of Colloid and Interface Science* **2015,** *446*, 185-193.

43. Ma, H.; Hradisky, M.; Johnson, W. P. Extending Applicability of Correlation Equations to Predict Colloidal Retention in Porous Media at Low Fluid Velocity. *Environ. Sci. Technol.* **2013,** *47* (5), 2272-2278.

44. Pazmino, E. F.; Trauscht, J.; Dame, B.; Johnson, W. P. Power Law Size-Distributed Heterogeneity Explains Colloid Retention on Soda Lime Glass in the Presence of Energy Barriers. *Langmuir* **2014,** *30* (19), 5412-5421.

45. Boccardo, G.; Marchisio, D. L.; Sethi, R. Microscale simulation of particle deposition in porous media. *Journal of Colloid and Interface Science* **2014,** *417* (0), 227-237.

46. Long, W.; Hilpert, M. A Correlation for the Collector Efficiency of Brownian Particles in Clean-Bed Filtration in Sphere Packings by a Lattice-Boltzmann Method. *Environ. Sci. Technol.* **2009,** *43* (12), 4419-4424.

47. Happel, J. VISCOUS FLOW IN MULTIPARTICLE SYSTEMS - SLOW MOTION OF FLUIDS RELATIVE TO BEDS OF SPHERICAL PARTICLES. *Aiche J.* **1958,** *4* (2), 197-201.

48. Nelson, K. E.; Ginn, T. R. Colloid Filtration Theory and the Happel Sphere-in-Cell Model Revisited with Direct Numerical Simulation of Colloids. *Langmuir* **2005,** *21* (6), 2173-2184.

49. Molnar, I. L.; Willson, C. S.; O'Carroll, D. M.; Rivers, M. L.; Gerhard, J. I. Method for Obtaining Silver Nanoparticle Concentrations within a Porous Medium via Synchrotron X-ray Computed Microtomography. *Environ. Sci. Technol.* **2014,** *48* (2), 1114-1122.

50. Cardenas, M. B. Three-dimensional vortices in single pores and their effects on transport. *Geophysical Research Letters* **2008,** *35* (18), L18402.

51. Torkzaban, S.; Tazehkand, S. S.; Walker, S. L.; Bradford, S. A. Transport and fate of bacteria in porous media: Coupled effects of chemical conditions and pore space geometry. *Water Resour. Res.* **2008,** *44* (4).

52. Li, Z.; Zhang, D. X.; Li, X. Tracking colloid transport in real pore structures: Comparisons with correlation equations and experimental observations. *Water Resour. Res.* **2012,** *48* (5), W05533.

53. Kocur, C. M.; Chowdhury, A. I.; Sakulchaicharoen, N.; Boparai, H. K.; Weber, K. P.; Sharma, P.; Krol, M. M.; Austrins, L.; Peace, C.; Sleep, B. E.; O'Carroll, D. M. Characterization of nZVI Mobility in a Field Scale Test. *Environ. Sci. Technol.* **2014,** *48* (5), 2862-2869.

54. Sakulchaicharoen, N.; O'Carroll, D. M.; Herrera, J. E. Enhanced stability and dechlorination activity of pre-synthesis stabilized nanoscale FePd particles. *Journal of Contaminant Hydrology* **2010,** *118* (3–4), 117-127.

55. Oh, W.; Lindquist, W. B. Image thresholding by indicator kriging. *Ieee Transactions on Pattern Analysis and Machine Intelligence* **1999,** *21* (7), 590-602.

56. Bhattad, P.; Willson, C. S.; Thompson, K. E. In *Segmentation of low-contrast three-phase X-Ray Computed Tomography images of porous media*, Proceedings of the GeoX 2010: 3rd International Workshop on X-ray CT for Geomaterials, New Orleans, LA, 2010; Alshibli, K.; Reed, A. H., Eds., pp 254-261.

57. Thompson, K. E.; Willson, C. S.; Zhang, W. L. Quantitative computer reconstruction of particulate materials from microtomography images. *Powder Technology* **2006,** *163* (3), 169-182.

58. Thompson, K. E.; Willson, C. S.; White, C. D.; Nyman, S. L.; Bhattacharya, J. P.; Reed, A. H. Application of a new grain-based reconstruction algorithm to microtomography images for quantitative characterization and flow modeling. *Spe Journal* **2008,** *13* (2), 164-176.

59. Lane, N. M. Numerical studies of flow in porous media using an unstructured approach. Doctor of Philosophy, Louisiana State University, December 2011.

60. Takbiri Borujeni, A.; Lane, N. M.; Thompson, K.; Tyagi, M. Effects of image resolution and numerical resolution on computed permeability of consolidated packing using LB and FEM pore-scale simulations. *Computers & Fluids* **2013,** *88* (0), 753-763.

61. Sanematsu, P.; Shen, Y.; Thompson, K.; Yu, T.; Wang, Y.; Chang, D.-L.; Alramahi, B.; Takbiri-Borujeni, A.; Tyagi, M.; Willson, C. Title: Image-based Stokes flow modeling in bulk proppant packs and propped fractures under high loading stresses. *Journal of Petroleum Science and Engineering* **2015**.

901 62. O'Carroll, D. M.; Bradford, S. A.; Abriola, L. M. Infiltration of PCE in a system containing spatial
902 wettability variations. *Journal of Contaminant Hydrology* **2004,** *73* (1-4), 39-63.
903 63. Elimelech, M. PARTICLE DEPOSITION ON IDEAL COLLECTORS FROM DILUTE FLOWING
904 SUSPENSIONS - MATHEMATICAL FORMULATION, NUMERICAL-SOLUTION, AND SIMULATIONS. *Sep.*
905 *Technol.* **1994,** *4* (4), 186-212.
906 64. Willson, C.; Lu, N.; Likos, W. Quantification of Grain, Pore, and Fluid Microstructure of
907 Unsaturated Sand from X-Ray Computed Tomography Images. *Geotechnical Testing Journal* **2012,** *35* (6),
908 1-13.
909 65. Pazmino, E. F.; Ma, H. L.; Johnson, W. P. Applicability of Colloid Filtration Theory in Size-
910 Distributed, Reduced Porosity, Granular Media in the Absence of Energy Barriers. *Environ. Sci. Technol.*
911 **2011,** *45* (24), 10401-10407.
912 66. Ma, H.; Johnson, W. P. Colloid Retention in Porous Media of Various Porosities: Predictions by
913 the Hemispheres-in-Cell Model. *Langmuir* **2009,** *26* (3), 1680-1687.
914 67. Seetha, N.; Majid Hassanizadeh, S.; Mohan Kumar, M. S.; Raoof, A. Correlation equations for
915 average deposition rate coefficients of nanoparticles in a cylindrical pore. *Water Resour. Res.* **2015**, n/a-
916 n/a.
917 68. Long, W.; Huang, H.; Serlemitsos, J.; Liu, E.; Reed, A. H.; Hilpert, M. Pore-scale study of the
918 collector efficiency of nanoparticles in packings of nonspherical collectors. *Colloids and Surfaces A:*
919 *Physicochemical and Engineering Aspects* **2010,** *358* (1–3), 163-171.
920 69. *Environmental and human health impacts of nanotechnology [electronic resource] / edited by*
921 *Jamie R. Lead, Emma Smith*.
922 70. Ma, H.; Johnson, W. P. Colloid Retention in Porous Media of Various Porosities: Predictions by
923 the Hemispheres-in-Cell Model. *Langmuir* **2010,** *26* (3), 1680-1687.
924 71. Ma, H.; Pazmino, E.; Johnson, W. P. Surface Heterogeneity on Hemispheres-in-Cell Model Yields
925 All Experimentally-Observed Non-Straining Colloid Retention Mechanisms in Porous Media in the
926 Presence of Energy Barriers. *Langmuir* **2011,** *27* (24), 14982-14994.
927 72. Kocur, C. M.; O'Carroll, D. M.; Sleep, B. E. Impact of nZVI stability on mobility in porous media.
928 *Journal of Contaminant Hydrology* **2013,** *145* (0), 17-25.
929 73. Bai, R.; Tien, C. Particle Deposition under Unfavorable Surface Interactions. *Journal of Colloid*
930 *and Interface Science* **1999,** *218* (2), 488-499.
931 74. Elimelech, M.; Omelia, C. R. EFFECT OF PARTICLE-SIZE ON COLLISION EFFICIENCY IN THE
932 DEPOSITION OF BROWNIAN PARTICLES WITH ELECTROSTATIC ENERGY BARRIERS. *Langmuir* **1990,** *6* (6),
933 1153-1163.
934 75. Tiraferri, A.; Sethi, R. Enhanced transport of zerovalent iron nanoparticles in saturated porous
935 media by guar gum. *J. Nanopart. Res.* **2009,** *11* (3), 635-645.

936